

Cobalt Single Atoms Anchored on Oxygen-Doped Tubular Carbon Nitride for Efficient Peroxymonosulfate Activation: Simultaneous Coordination Structure and Morphology Modulation

Ziwei Wang,^[a] Eydhah Almatrafi,^[b] Han Wang,^[a] Hong Qin,^[a] Wenjun Wang,^[a] Li Du,^[a] Sha Chen,^[a] Guangming Zeng,^{*,[a, b]} Piao Xu,^{*,[a, b]}

[a] Dr. Z. W. Wang, Dr. H. Wang, Dr. H. Qin, Dr. W. J. Wang, Dr. L. Du, Dr. S. Chen, Prof. G.M. Zeng, Prof. P. Xu
College of Environmental Science and Engineering, Hunan University and Key Laboratory of Environmental Biology and Pollution Control (Ministry of Education)
Hunan University
Changsha 410082, P.R. China
E-mail: zgming@hnu.edu.cn (G. Zeng)

[b] Prof. E. Almatrafi, Prof. G.M. Zeng, Prof. P. Xu
Centre of Research Excellence in Renewable Energy and Power Systems, Center of Excellence in Desalination Technology, Department of Mechanical Engineering, Faculty of Engineering-Rabigh
King Abdulaziz University
Jeddah 21589, Saudi Arabia

Abstract: Simultaneous regulation of the coordination environment of single-atom catalysts and engineering architectures with efficient exposed active sites are efficient strategies for boosting peroxymonosulfate (PMS) activation. We isolated cobalt atoms with dual nitrogen and oxygen coordination (Co-N₂O₂) on oxygen-doped tubular carbon nitride (TCN) by pyrolyzing a hydrogen-bonded cyanuric acid melamine-cobalt acetate precursor. The theoretically constructed Co-N₂O₂ moiety on TCN exhibited an impressive mass activity of 7.61×10⁵ min⁻¹ mol⁻¹ with high ¹O₂ selectivity. Theoretical calculations revealed that the cobalt single atoms occupied a dual nitrogen and oxygen coordination environment, and that PMS adsorption was promoted and energy barriers reduced for the key *O intermediate that produced ¹O₂. The catalysts were attached to a widely used poly(vinylidene fluoride) microfiltration membrane to deliver an antibiotic wastewater treatment system with 97.5% ciprofloxacin rejection over 10 hours, thereby revealing the suitability of the membrane for industrial applications.

Introduction

Advanced oxidation processes (AOPs), especially for the peroxymonosulfate (PMS) activation, are state-of-the-art wastewater treatment technologies for water decontamination.^[1] Its removal of recalcitrant organic contaminants relies on the highly reactive radicals (*OH and SO₄^{•-}) or alternative nonradical pathways.^[2] Among the alternative nonradical pathways, singlet oxygenation has received tremendous attention as its intrinsic advantages of long life, wide pH tolerance, strong electrophilicity and selectivity.^[3] As a result, singlet oxygenation in PMS-AOPs displays high selectivity toward electron-rich organic substances or bacteria and maintains excellent efficiency in complicated environmental interference.^[4] In general, the singlet oxygen (¹O₂) forms via self-decay, nucleophilic addition, and catalytic activation of peroxy acids like PMS.^[5] Many carbonaceous materials such as carbon nanotubes^[6] and biochar^[7] as well as transition metal-based catalysts^[8] are efficient activators for PMS-AOPs towards ¹O₂ generation, but the process is usually accompanied by the production of free radicals such as *OH and

SO₄^{•-}. Furthermore, their practical application in environment remediation still suffers from poor stability, low atomic utilization efficiency, and slow activation kinetics.

Co single-atom catalysts (SACs) with atomically dispersed active sites are one of the most promising catalysts for PMS-AOPs due to significantly promoted catalytic properties, well-defined structure and the highest reactivity of Co²⁺.^[9] Firstly, compared to metal nanocrystals or oxides, single atoms possess greater atomic utilization and mass activity toward PMS activation.^[8, 10] For example, the reaction rate of Co-N-C single atoms on tetrapyridomacrocyclic support for PMS activation is 2 to 4 orders of magnitude higher than that of Co²⁺ and Co₃O₄ catalysts.^[11] Secondly, the rational design of SACs can further modulate the reaction pathway towards ¹O₂ production.^[9a] Lately, the transformation of Co-N₄-C structure to Co-N₂₊₂-C coordination has obtained with more than 98% ¹O₂ generation selectivity for PMS activation.^[12] Therefore, defining single-atom sites at atomic level and constructing the macrostructures of the whole catalyst can synergistically enhance PMS-AOPs catalytic efficiency and ¹O₂ production selectivity. However, the investigation of the structure-property relationships is highly fascinating yet difficult.

In general, the catalytic performance of Co-SACs is simultaneously determined by isolated metal atoms, their local coordination environment and support architectures.^[13] The N atoms on the support not only anchor the metal atoms but also modulate the electronic structures of the active centers.^[14] Therefore, the replacement of N atoms with other atoms (e.g. O and S) can alter the electronic structure of the active sites, further promoting the turnover frequencies and boosting catalytic activity.^[15] For instance, June et al.^[16] synthesized Co single atoms on N, O doped graphene support and Qiao et al.^[17] explored the effects of oxygen-adjacent Co single atoms on the oxygen reduction reaction (ORR). These findings verified the optimized Co-N₄ moiety obtained by incorporating O-adjacent C atom displayed superior ORR activity and high H₂O₂ productivity, originating from the active site shift and modulation. Furthermore, the rationally engineering architectures of support can enhance surface area and porosity, thus enabling the maximum exposure of the active sites.^[18] In PMS-AOPs, oxygen-doped carbon nitrogen (CN) and Co-SACs (Co-N₄ moiety) both have been studied as efficient catalysts.^[10e, 19] However, simultaneously

modulating the local coordination environment of Co single atoms and support architectures of CN has few been reported regarding PMS-AOPs, which further leads to a poor understanding of reaction mechanisms, and structure–property relationships.

Herein, we designed a supramolecular precursor to prepare isolated Co atoms with N, O-dual coordination on oxygen doped tubular CN as an effective activator for PMS-AOPs. The single Co atom dispersion and tubular filling-like porous architecture provided abundant exposed active sites and sufficient interaction with PMS as well as related activation intermediates, resulting in high PMS activation ability and selectivity for $^1\text{O}_2$ generation. Theoretical calculation revealed that O-adjacent Co-SACs could indeed alter PMS adsorption configuration and reduce energy barriers of key *O intermediate toward $^1\text{O}_2$ production. We further illustrated the immobilization of the catalysts in a poly(vinylidene fluoride) microfiltration membrane to establish a continuous flow system. Intriguingly, this study details the insights into the Co-SACs with molecular-level engineering for efficient and sustainable wastewater remediation.

Results and Discussion

It is established that the adsorption energy (E_{ads}) of PMS and the O–O bond length ($l_{\text{O–O}}$) in the PMS molecular have a direct impact on PMS activation.^[4, 20] Typically, E_{ads} controls the thermodynamic feasibility of an adsorption process and indicates the interactions between catalysts and PMS, while the $l_{\text{O–O}}$ reflects the feasibility of PMS cleavage.^[21] Therefore, we conducted periodic DFT calculations to investigate the impact of molecular-level local structures of Co- N_4/CN (Co- N_4) catalyst on PMS activation, including the prevalent Co_3O_4 , CN, oxygen doped CN and various configurations of Co-SACs at molecular level (modulation of the first coordination sphere, such as B, O, S, P, namely Co- N_3B , Co- N_3O , Co- N_3S , Co- N_3P). The E_{ads} and $l_{\text{O–O}}$ on different models were shown in Figure 1a, Figure S1 and Table S1. We found that PMS $^{\cdot-}$ energetically preferred to be adsorbed by Co- N_3O moiety and Co_3O_4 , whereas the former Co-SACs prefer breaking the O–O bond of PMS molecule, which leads to active species formation. Additionally, Figure 1b showed the formation energy of Co- N_4 moiety in a unit of g- C_3N_4 and the formation energy of two possible coordination environment (named Co- N_3O_1 and Co- $\text{N}_4\text{–O}$) in a unit of oxygen doped g- C_3N_4 . Compared to the Co- N_4 moiety and Co- $\text{N}_4\text{–O}$ (oxygen in the second coordination sphere), the formation energy of Co- N_3O_1 reduced from 2.14 eV and -2.03 eV to -2.44 eV respectively, indicating a more feasible coordinated position.

Guided by the analysis from theoretical calculations, the attention of this article focused on Co-SACs on oxygen-doped carbon nitride. It was reported that hydrothermal treatment could simultaneously dope oxygen atoms into CN and regulate the architectures.^[22] The preparation process was presented in Figure 1c. The melamine supramolecular precursors were synthesized under hydrothermal conditions, which underwent a self-assembly process into hydrogen bonding cyanuric acid-melamine.^[23] Then, the supramolecular precursors were calcinated to generate nanotube structure (TCN, height ~1.18 μm) during high temperature (AFM, Figure 1d, TEM and SEM, Figure S2a). Meanwhile, the coordinated cobaltous nodes were reduced by the generated abundant reductive atmosphere

during calcination. Pre-mediated coordination of cobaltous acetate and supramolecular precursors could change the distance of adjacent Co atoms, thus preventing the aggregation of Co atoms and the construction of Co–Co bonds (TEM Figure 1e, f).^[24] No clear change of morphology was found after calcination with addition of cobaltous acetate (Figure S2b–f). Furthermore, isolated single Co atoms (assigned by bright spots) were obviously observed anchoring on the internal architecture (HAADF-STEM, Figure 1g, TEM, Figure S3, S4). The engineering support architecture relies on morphology controls (along with oxygen atoms introduction) and subsequently uncoordinated metal-ligand removal from precursors. The incorporation of oxygen atoms into supramolecular precursors provided abundant surface anchoring sites for metal atoms and efficiently reduced the formation energy for Co-SACs.^[25] Furthermore, the associated interactions between the precursors and metal atoms finely controlled the spatial location between adjacent Co atoms, which were further in favor of Co-SACs formation.^[26] EDS mapping across a part of nanotube (Figure 1h) suggested the homogeneous distribution of N, C, O, Co over Co- N_3O_1 matrix. As proof of concept, the pyrolysis of the precursors synthesized by ball-milling of melamine, cyanuric acid and cobaltous acetate indeed had the desired effects (Figure S5).

The crystal structures of CN, Co- N_4 , TCN, Co- N_3O_1 were illustrated by XRD (Figure S6a). Two characteristic peaks at 13.4° and 25.6° were ascribed to (110) and (200) facets of origin CN. As can be seen, TCN and Co- N_3O_1 maintained the basic skeleton of carbon nitride, which was also proved in the (FT-IR) spectra (Figure S6b). The absence of characteristic peaks of cobalt species, such as cobalt crystal, cobaltous oxides further agreed with HAADF-STEM results. While for TCN and Co- N_3O_1 , the reflection peaks of (200) facets shifted to a higher angle, indicating that the incorporation of O heteroatom atoms might distribute the packing of the singlet layers of CN.^[27] The enhanced paramagnetic signal with a g value of 2.003 further supported that oxygen atoms were introduced into TCN (Figure S7a). The surface area of Co- $\text{N}_3\text{O}_1\text{–3}$ was 83.11 m^2/g , which was about 2.08 and 8.33 times than that of TCN and CN (Figure S7b, Table S2). This was because the tubular structure enhanced the accessible surface area and the introduction of Co atoms within the framework generated more porous architecture. According to the ICP-MS measurement, the Co content for Co- N_4 , Co- $\text{N}_3\text{O}_1\text{–1}$, Co- $\text{N}_3\text{O}_1\text{–2}$ and Co- $\text{N}_3\text{O}_1\text{–3}$ were 0.99, 0.51, 3.08 and 10.49 wt%, respectively (Table S2).

To investigate the chemical position and electronic structures of CN, TCN Co- N_4 and Co- N_3O_1 , XPS spectra was performed. Through the comparison among the high-resolution C 1s, O 1s of CN and TCN, two variations could be observed in this spectrum and were emphasized by differently shaded regions in Figure 2a, b. The peaks at C 1s and O 1s corresponding to C–O groups exhibited a clear increase in the intensity while the C–N=C species existent in TCN was found to be lower than that of CN, confirming that the presence of trace amounts of sp^2 -hybridized N atoms substituted by O atoms in the C-containing triazine rings.^[28] Several reports have also proved this observation that the doped O atoms are favorable for the substitution of two-coordinated N atoms.^[19a] Given the difference in electronegativity between O atoms and N atoms, this change would alter the electronic structure of TCN and further have a direct impact on the coordination environment of single Co atoms. As shown in Figure S8 and Table S3, correlation of Co loadings with different O and N contents across

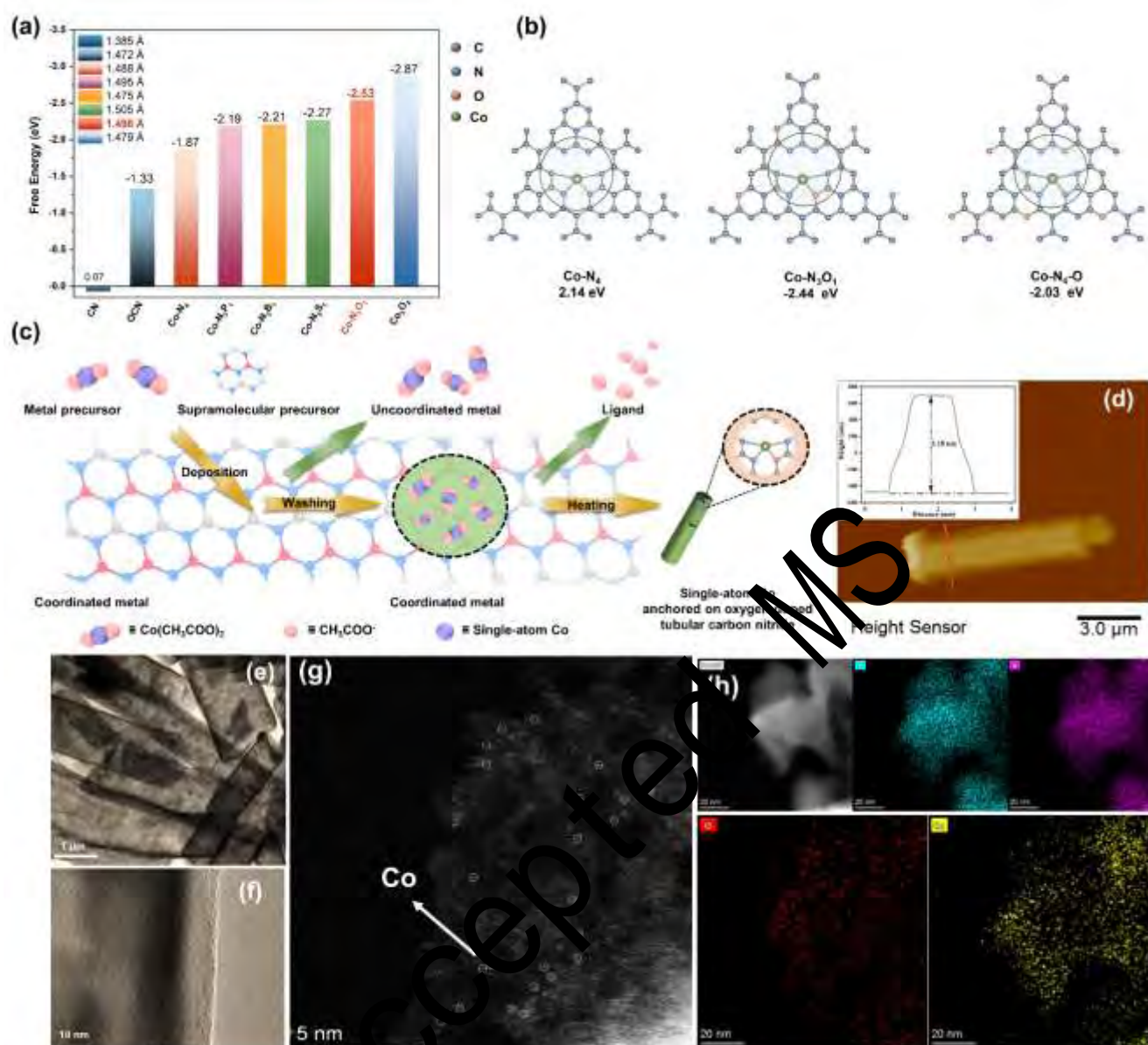


Figure 1. (a) The adsorption energy (E_{ads}) of PMS on prevalent Co₃O₄, carbon nitrogen and oxygen doped carbon nitrogen and various configurations at the molecular level of Co-N₄ moiety (in the first coordination sphere, such as B, O, S, P, etc.) and the corresponding O-O bond length ($l_{\text{O-O}}$) in PMS after adsorption (b) calculated formation energy of Co-N₄ and different O-adjacent Co-SACs (Co-N₃O₁ and Co-N₄O). (c) Process of the formation of Co-N₃O₁, (d) AFM of TCN, (e) and (f) TEM images of Co-N₃O₁, (g) HAADF-STEM of Co-N₃O₁, (h) EDS mapping images of Co-N₃O₁.

all TCN matrix-based catalysts revealed that only C-O groups and C-N=C species exhibited a direct trend with Co loadings (the normalization method was adopted), indicating that the nucleation of Co mainly at N, O-dual related sites (Figure 2c). In comparison to Co-N₃O₁, the Co 2p spectrum of Co-N₄ displayed a downshift to lower binding energy and the spin-orbit splitting of Co-N₄ (15.32 eV) was smaller than that of Co-N₃O₁-Co (15.81 eV), indicating that Co-N₃O₁-Co possessed highly oxidized cobalt atom centers with a lower charge density state (Figure S9d).^[16]

X-ray absorption fine structure (XAFS) measurements were conducted to identify the possible chemical state and coordination environment of single Co atoms in Co-N₃O₁ and Co-N₄. As shown in Figure 2d, the X-ray absorption near edge structure (XANES) spectra of Co-N₃O₁ and references compounds indicated that the absorption edge (line position) of Co-N₃O₁ was close to that of CoO, suggesting the valence state

of Co species in Co-N₃O₁ resemble 2+. The Fourier transform (FT) EXAFS of Co-N₃O₁, Co-N₄ and reference samples revealed that Co species coordinated as isolated single atoms due to the absence of characteristic peaks of Co-Co (at 2.18 Å). Notably, a slight variation in the local coordination structures among samples was observed in FT EXAFS and wavelet transform (WT) analysis (Figure 2h-l) due to the shifts of the major peaks. One major peak (1.56 Å) for Co-N₃O₁ was located between the backscattering of Co-N (Co-N₄, CoPc) and Co-O (CoO), referring to the construction of Co-N, O dual coordination environment (Figure 2e).^[17, 19b] Consistent with the FT results, the Co-light-atoms bonds display upward shift due to the oxidation of Co atoms. These findings are consistent with proposed structure and a similar coordination configuration reported in 2021.^[14a, 16-17] To confirm the local coordination configurations to single Co atoms in prepared samples, the quantitative least-squares EXAFS curve-fitting analyses were

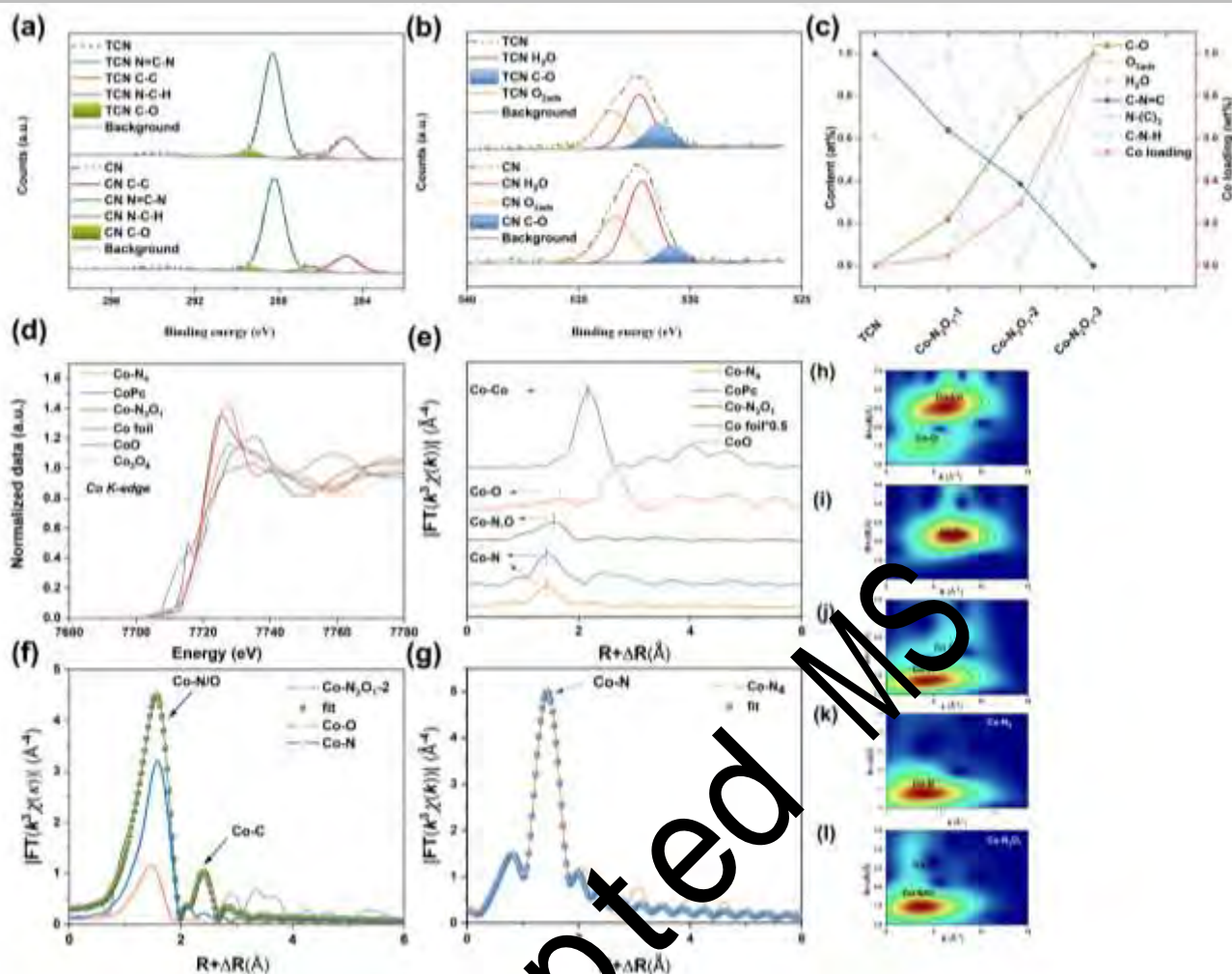


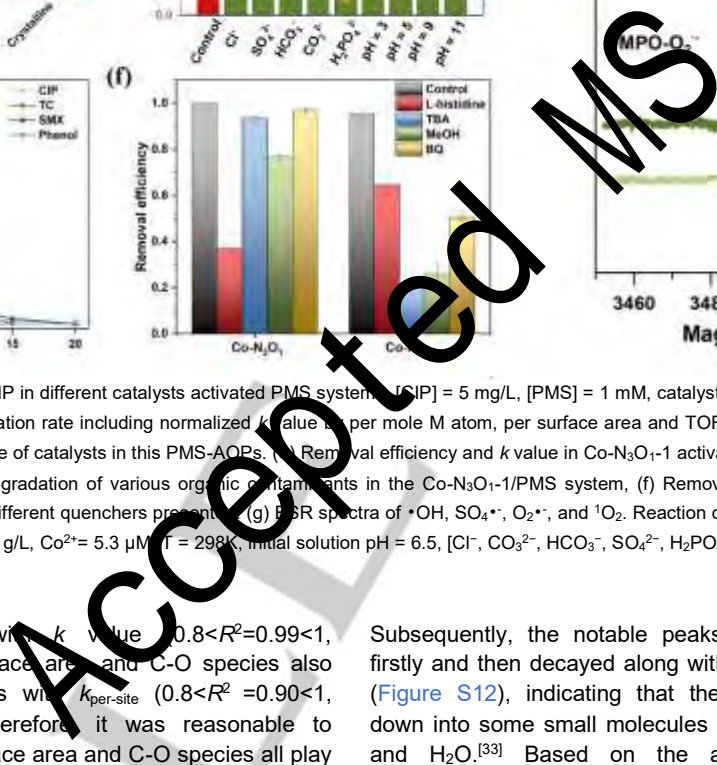
Figure 2. Devolution of (a) C 1s, (b) O 1s XPS spectra of TCN and Co-N₃O₁, (c) the contents of O and C functions according to XPS and the Co loadings in TCN and Co-N₃O₁ samples, (d) normalized Co K-edge XANES spectra of Co foil and the Co-based samples (e) Co K-edge FT-EXAFS spectra for Co-N₃O₁ and reference samples. Co K-edge EXAFS fitting analyses for Co-N₃O₁ in R space (f) and k space (g), (h-k) Co K-edge WT-EXAFS contour plots for Co-N₃O₁ and reference samples.

used to reveal the first shell of the Co atom. As displayed in Figure 2f and g, the best fitting results of Co-N₃O₁ showed a four-coordination number and contained Co-N and Co-O backscattering paths, which were different from the coordination number of Co-N (3.9±0.3) in Co-N₄. The corresponding number for N and O atoms were 3.1±0.5 and 1.0±0.3 at distance of 2.03 and 1.92 Å, suggesting the possible Co-N₃O₁ configuration. In addition, the result was further simulated based on the models of Co-N₂O₂, and Co-N₄O₃ (Figure S10, Table S4). It was shown that Co-N₃O₁ configuration presented a best agreement with the experimental data, further confirming the introduction of O atoms into Co-N₄ moieties.

The catalytic activity of Co-N₃O₁ as PMS-AOPs catalysts was evaluated by the oxidative degradation of CIP as a model reaction. As expected, all Co-N₃O₁ samples exhibited much higher catalytic degradation rate with CIP degradation efficiency up to 100% within 20 min (Figure 3a). Compared with Co-N₄-1 moiety (with similar Co-content), Co-N₃O₁-1 showed a obviously higher catalytic degradation rate. While < 80% CIP was decomposed when using Co₃O₄ as catalysts and the TCN or pristine PMS displayed negligible catalytic performance. To investigate the catalytic activity based on a quantitative comparison, we normalized the *k* value based on the mole ratio of metal contents (*k*_{per-site}), surface area (*k*_{surface area}) and used

turnover frequency (TOF) to fit CIP degradation process (Table S5).^[11] As shown in Figure 3b, the Co-N₃O₁-2 exhibited the highest normalized *k*_{per-site} value and TOF efficiency, which was up to 7.61×10⁵ min⁻¹ mol⁻¹ and 0.014 s⁻¹. All the Co-N₃O₁ catalysts possessed a higher normalized *k*_{per-site} value and TOF efficiency, indicating that per Co atom in Co-N₃O₁ had a higher reactivity for PMS activation than that of Co-N₄. The significantly enhanced normalized *k* value and TOF efficiency of Co-N₃O₁ and Co-N₄ structure compared to Co²⁺ and Co₃O₄ could be ascribed to the interaction between oxygen doped C₃N₄ matrix and single Co active centers.^[29] Although the configuration of Co-N₃O₁ presented superior activity towards PMS-AOPs compared to Co-N₄ moieties, some distinct indicators, such as different TOFs among the same configurations and the higher *k*_{surface area} value of Co-N₄-2 than that of Co-N₃O₁-1, suggested that other factors may all cause the activity difference.^[30]

To further investigate the origins of the catalyst's activity, the potential correlations between the effect factors and catalytic performance of catalysts in these PMS-AOPs were established (Figure 3c).^[31] The magnitude and degree of the correlation were represented by the shade of color and the size of circle, respectively. Furthermore, the number of asterisk referred to a significant level. Obviously, the index of Co loading displayed



Liquid chromatography-mass spectrometry (LC-MS) was performed to identify the degradation intermediates.^[32] As displayed in [Figure S11](#), the chromatograms of a 5 mg/L CIP solution at different reaction times were presented. The labeled peaks are corresponding to CIP with $m/z = 332$ at retention time 10.7 min and major degradation intermediates with $m/z = 348$ at retention time 4.5 min. The peaks of CIP decayed rapidly with the reaction time finally disappeared after 20 min. The results were consistent with the degradation experiment ([Figure 3a](#)).

The PMS activation ability of Co-N₃O₁-1 was further evaluated by the degradation of multiple contaminants (e.g., sulfamethoxazole, tetracycline, and phenol) ([Figure 3e](#)). All

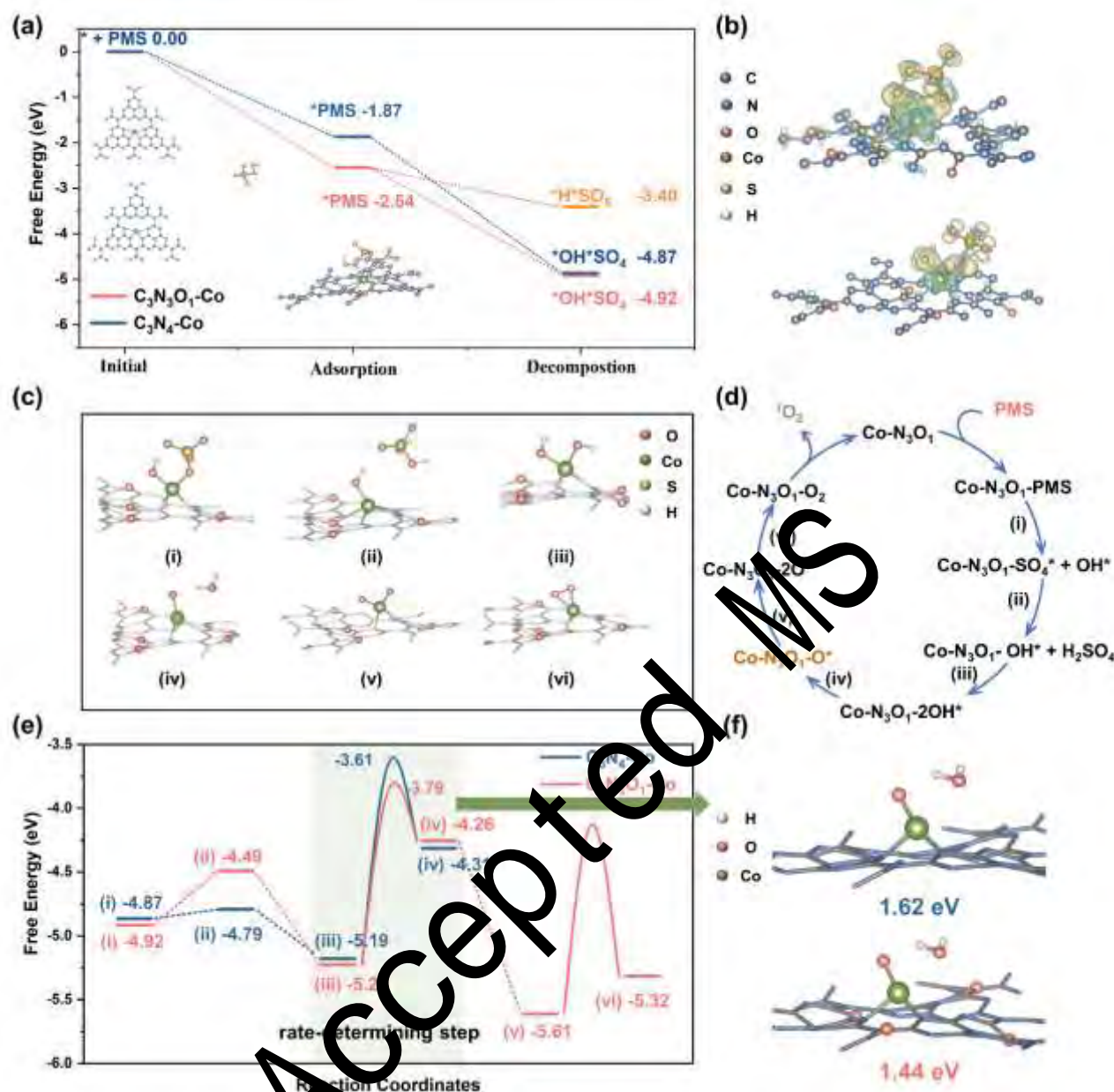


Figure 4. Proposed mechanism of $^1\text{O}_2$ generation over $\text{Co-N}_3\text{O}_1$ via PMS activation by DFT methods. (a) Calculated potential energy diagrams for PMS decomposition to two key reaction intermediates and Gibbs free energy comparison of $\text{Co-N}_3\text{O}_1$ and Co-N_4 towards PMS adsorption, (b) Bader charge analysis of two key reaction intermediates on $\text{Co-N}_3\text{O}_1$, (c) The corresponding structures of reaction intermediates for proposed reaction process. (d) Proposed reaction process for SO_4^* and OH^* moieties oxidation to $^1\text{O}_2$ on $\text{Co-N}_3\text{O}_1$ catalysts. (e) The calculated potential energy diagrams for the rate-determining step and transition state based on SO_4^* and OH^* moieties oxidation to $^1\text{O}_2$ on $\text{Co-N}_3\text{O}_1$ and Co-N_4 catalysts. (f) The kinetic barriers for 2^*OH to $^*\text{O}$ on $\text{Co-N}_3\text{O}_1$ and Co-N_4 catalysts.

contaminants were completely decomposed by $\text{Co-N}_3\text{O}_1$ -1/PMS system in 20 min. Increasing the catalyst dosage or PMS concentration both improved the catalytic efficiency, indicating the high utilization efficiency of $\text{Co-N}_3\text{O}_1$ -1/PMS system (Figure S16b, c). Based on the PMS decomposition experiments, the PMS decomposition efficiency reached 71.68% and 89.71% for $\text{Co-N}_3\text{O}_1$ -1 and $\text{Co-N}_3\text{O}_1$ -2, respectively (Figure S16d). All the above analyses suggested that $\text{Co-N}_3\text{O}_1$ was a promising PMS activator, in which the specific interaction between single Co atoms and oxygen doped tubular C_3N_4 provided an accelerated activation pathway compared to Co^{2+} ions (homogeneous process) and Co-N_4 moiety (heterogeneous process).

Engineering the coordination environment of single atoms has been proved as an efficient strategy to selectively generate

active radicals.^[14b] To identify the dominated active species generated in these systems, radical quenching experiments were employed. ESR characterizations were employed as a direct monitor by using TEMP and DMPO as trapping agents. As shown in Figure 3g, the intensity of the triplet signals of TEMO- $^1\text{O}_2$ in $\text{Co-N}_3\text{O}_1$ /PMS system was significantly enhanced compared to Co-N_4 /PMS system. Furthermore, only DMPO- $^*\text{OH}$ and slight DMPO- $\text{O}_2^{\cdot-}$ were detectable in Co-N_4 /PMS system, indicating that $\text{Co-N}_3\text{O}_1$ /PMS system was highly selective to generate $^1\text{O}_2$, which was further proved by the radical quenching experiments. When TBA, methanol and BQ were added into the $\text{Co-N}_3\text{O}_1$ reaction process, only a negligible inhibition ratio of CIP decomposition could be observed (Figure 3f). Furthermore, L-histidine and NaN_3 significantly inhibited the CIP

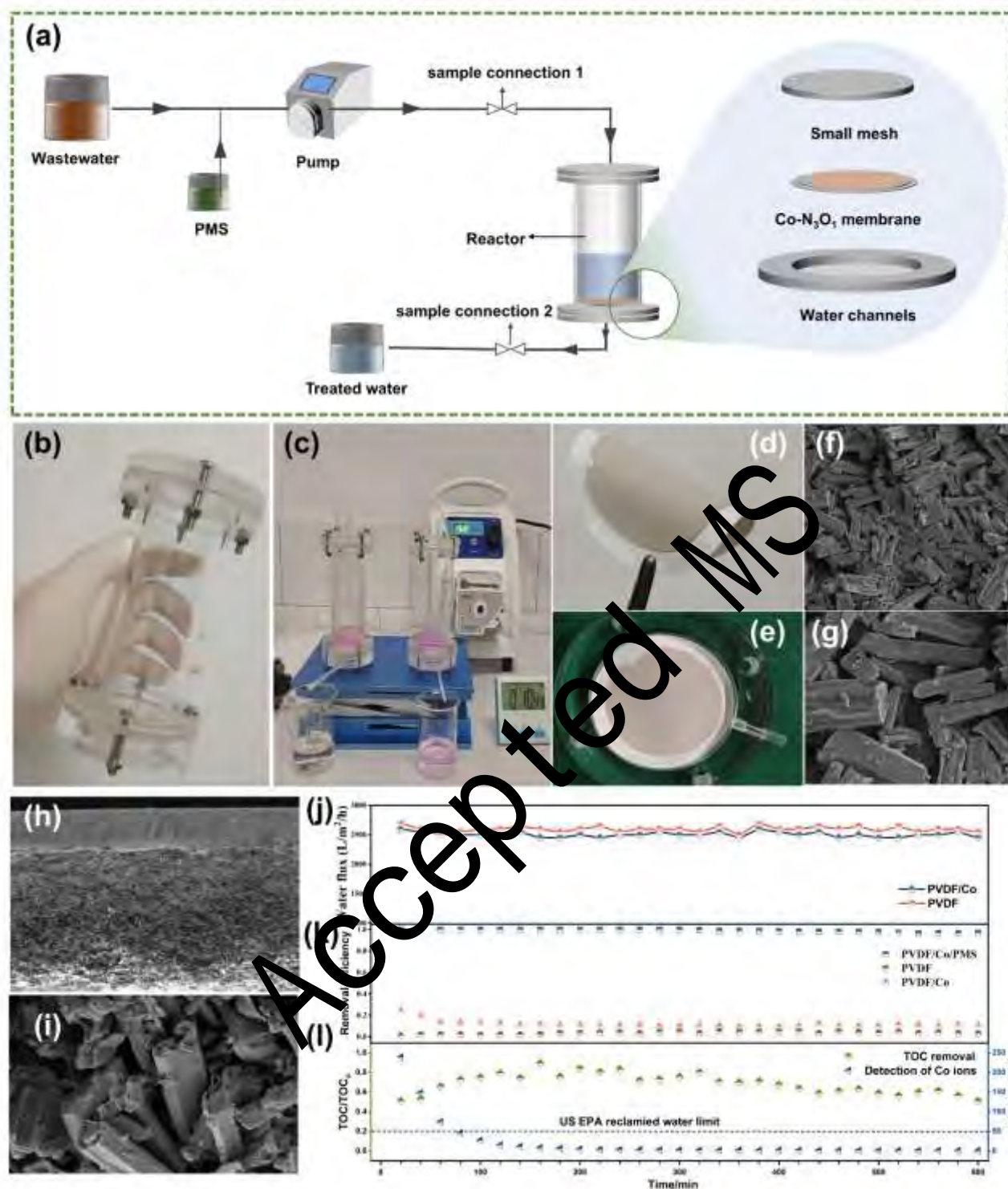


Figure 5. Preparation of Co-N₃O₁ membranes and application in water treatment via a continuous flow system. (a) Schematic illustration of wastewater treatment process, (b, c) Photograph of experiment device. To act as a proof-of-concept, the CIP was replaced as RhB for better observation, (d, e) Photograph of the prepared Co-N₃O₁ membranes with an area of 12.56 cm² and the membrane exhibit high flexibility, (f, g) SEM images of membrane surfaces, (h, i) Cross-sectional scanning electron micrographs of membrane, (j) the water performance of Co- N₃O₁ membranes and pristine membranes, (k) CIP removal efficiency using Co-N₃O₁ membranes and pristine membranes (l) TOC removal and Co concentration in effluent as functions of filtration time.

decomposition, and the higher concentrations of L-histidine and NaN₃ could cause a higher inhibition effect (Figure S17a). In the contrast, both TBA and methanol significantly inhibited the CIP degradation in the Co-N₄/PMS system, while L-histidine had a weak effect on the reaction process. With the structure change from Co-N₄ moiety to Co-N₃O₁ moiety, the inhibition of L-

histidine increased from 35.28% to 63.05%, while the inhibition of TBA decreased from 78.71% to 6.73% (Figure 3e). Note that other factors such as the interaction between PMS and L-histidine,^[34] PMS self-decomposition,^[32] electron transfer^[4, 35] et al. could have an impact on the degradation process. Throughout a series of experiment under different conditions

(Figure S17 and S18), we further identified that $^1\text{O}_2$ were dominant radicals and the origin relied on PMS activation by $\text{Co-N}_3\text{O}_1$. These findings confirmed that incorporation of oxygen atoms into Co-SACs local coordination environment favoured selective generation of $^1\text{O}_2$.

The possible pathway towards selective $^1\text{O}_2$ production mechanism was further explored by the DFT computations. Based on the new insights into the activation of PMS towards $^1\text{O}_2$ production, we focused on two different reaction intermediates.^[19b] The first pathway was the loss of the H atom to generate SO_5^* and then the SO_5^* rapidly self-reaction to produce $^1\text{O}_2$, SO_4^{2-} and $\text{S}_2\text{O}_8^{2-}$. In another pathway, the PMS was divided into SO_4^* and OH^* moieties. The free energy profiles demonstrated that $\text{PMS} \rightarrow \text{PMS}^* \rightarrow \text{SO}_4^* + \text{OH}^*$ were more thermodynamically favorable (Figure 4a). Bader charge change of divided SO_4^* and OH^* (1.41 e^-) was much more than that of divided SO_5^* and H^* (1.06 e^-), confirming the second pathway allowed donating more electrons to adsorbed PMS (Figure 4b, Table S7), which was also proved by LSV analyses (Figure S19). The results of the decreased current indicated that electrons transferred from a single Co atom to PMS. Compared to Co-N_4 moiety, the changed current density of $\text{Co-N}_3\text{O}_1$ was much higher, suggesting that $\text{Co-N}_3\text{O}_1$ manifested a better conductivity for electron migration and possessed a faster reaction rate.^[6] Furthermore, the charge state of the cobalt atom in Co-SO_4^* (active sites) became more positive by 0.05 e^- in comparison with Co-SO_5^* , hinting that SO_4^* and OH^* could slightly increase the charge state of the cobalt atom.^[14b]

To distinguish the different selectivity towards reactive species generation between $\text{Co-N}_3\text{O}_1$ and Co-N_4 , optimized potential free energy diagrams for the $^1\text{O}_2$ generation were then shown in Figure 4c, d, namely, $\text{PMS} \rightarrow \text{PMS}^* \rightarrow \text{SO}_4^* + \text{OH}^* \rightarrow \text{OH}^* + \text{H}_2\text{SO}_4 \rightarrow 2\text{OH}^* \rightarrow \text{O}^* \rightarrow 2\text{O}^* \rightarrow ^1\text{O}_2$. For this typical pathway, the OH^* was adsorbed on the single Co atom site while SO_4^* was employed to form H_2SO_4 via an exothermic reaction. In this step, Co-N_4 moiety presented reaction energy of -4.79 eV compared to that for $\text{Co-N}_3\text{O}_1$ of -4.40 eV , demonstrating that SO_4^* may play more important roles under the effects of O atoms (Figure 4e). Furthermore, both the free energy diagram of $\text{Co-N}_3\text{O}_1$ and Co-N_4 moiety showed the largest energy barrier for the $^*\text{O}$ intermediate formation during the multistep $^1\text{O}_2$ generation process, indicating the formation of $^*\text{O}$ intermediate was a rate-determining step. After oxygen incorporation, the energy barrier regarding $^*\text{O}$ intermediate formation of $^*\text{O}$ intermediate was reduced from 1.62 eV to 1.44 eV , accounting for the promoted $^1\text{O}_2$ generation energetics (Figure 4f). The above theoretical results revealed that incorporation of oxygen atoms into the coordination environment of single Co atoms would alter the electronic structure of Co centers, thus contributing to promoting adsorption of PMS molecules and thermodynamically generating $^*\text{O}$ intermediate toward fast and selective $^1\text{O}_2$ generation.

Given the excellent catalytic performance of $\text{Co-N}_3\text{O}_1/\text{PMS}$ system, it was further used in a practical application (Figure 5a, b, c). Membrane technology has created a bright future for supplying clean water resources due to its sustainability and convenience compared to dispersed catalyst suspensions.^[36] The $\text{Co-N}_3\text{O}_1$ membranes were fabricated by vacuum-assisted filtering $\text{Co-N}_3\text{O}_1$ suspensions via PVDF substrate, namely PVDF/Co (Figure 5d, e). As shown in Figure 5f, g, the PVDF/Co was flexible and elastic. SEM images displayed that the random stacking of $\text{Co-N}_3\text{O}_1$ without obvious cracks and the cross-sectional SEM images indicated the PVDF/Co membranes had

a thickness of about $217\text{ }\mu\text{m}$ with accessible 2D pinholes (Figure 5h, i). These abundant self-tubular structures with nanoholes can be employed as efficient water transfer channels, supplying full active catalytic sites for rapid permeation and purification of polluted water.

We firstly investigated CIP effluents permeances of PVDF and PVDF/Co to evaluate the transfer mass feature and rejection efficiency of target pollutant. The long-term performance was conducted by 30 cyclic tests over 10 h. The pristine membrane showed a water performance of $2594.29\text{ L/m}^2/\text{h}$ accompanied by nearly 3.41% (average) rejection over 10 h. Comparatively, PVDF/Co gave similar water permeance of $2502.85\text{ L/m}^2/\text{h}$ accompanied by nearly 11.30% (average) rejection, respectively (Figure 5j). These indicated that $\text{Co-N}_3\text{O}_1$ were efficient building blocks for water transportation and pollutants separation. After the addition of PMS, the removal of CIP in PVDF/Co system maintained 97.5% over 10h (Figure 5k), and the retention time of effluents in the PVDF/Co was only 312 ms (Figure S20), suggesting the high activity of PVDF/Co towards PMS activation.

Another advantage of PVDF/Co-based reactors lied in their leaching resistance and mineralization ability. As shown in Figure 5l, the detected Co concentration in the PVDF/Co/PMS system was at a state of $46.096\text{ }\mu\text{g/L}$ after the fourth cycle, which was lower than the limitation of reclaimed water set by the US Environmental Protection Agency ($50\text{ }\mu\text{g/L}$). In the last few cycles, the detection leaching was below the $1\text{ }\mu\text{g/L}$, suggesting the strong coordination between single Co atoms and C_3N_4 . The TOC mineral efficiency in the effluent was more than 51.10% throughout the process of PVDF/Co/PMS experiment, indicating the efficient oxidation of the CIP molecules.

Conclusion

The modulation of coordination environment and design of support architectures can be adopted as new design principles for SACs toward PMS activation. In this study, the $\text{Co-N}_3\text{O}_1$ moiety anchored on TCN combined the advantages of PMS activation and selective $^1\text{O}_2$ generation process with robust stability. The per single-atom achieved a high k value of $7.61 \times 10^5\text{ min}^{-1}\text{ mol}^{-1}$ and TOF of 0.014 s^{-1} . Further integration of $\text{Co-N}_3\text{O}_1$ into membrane separation technology achieved high rejections ($> 97\%$) toward pollutants with water permeances of $2502.85\text{ L/m}^2/\text{h}$ above. Experiment and theoretical calculations revealed that the high PMS activation and selectivity for $^1\text{O}_2$ generation correlated with the incorporation of oxygen atoms into Co-SACs sites and morphology modulation, which resulted in the enhanced adsorption energy of PMS, enlarged contact surface area, and reduced activation barriers for $^1\text{O}_2$ generation. These findings provide a novelty design principle for single atom-based nanomaterials and highlight the reaction mechanism of PMS activation at the molecular level.

Acknowledgements

This work was supported by the National Natural Science Foundation of China (82003363, 82073449, U20A20323, 51521006, 52070077), the National Program for Support of Top-Notch Young Professionals of China (2014), the Program for Changjiang Scholars and Innovative Research Team in University (IRT-13R17), the Three Gorges Follow-up Research Project (2017HXXY-05), and the National Natural Science Foundation of Changsha (kq2007059).

Conflict of Interest

The authors declare no conflict of interest.

Keywords: single-atom catalysts • peroxymonosulfate activation • wastewater treatment • carbon nitride • coordination environment.

- [1] a) Q. Q. Zhang, G. G. Ying, C. G. Pan, Y. S. Liu, J. L. Zhao, *Environ Sci Technol* **2015**, *49*, 6772-6782; b) T. U. Berendonk, C. M. Manaia, C. Merlin, D. Fatta-Kassinos, E. Cytryn, F. Walsh, H. Bürgmann, H. Sørum, M. Norström, M.-N. Pons, N. Kreuzinger, P. Huovinen, S. Stefani, T. Schwartz, V. Kisand, F. Baquero, J. L. Martinez, *Nature Reviews Microbiology* **2015**, *13*, 310-317.
- [2] J. Lee, U. von Gunten, J. H. Kim, *Environ Sci Technol* **2020**, *54*, 3064-3081.
- [3] B. C. Hodges, E. L. Cates, J. H. Kim, *Nat Nanotechnol* **2018**, *13*, 642-650.
- [4] W. Ren, C. Cheng, P. Shao, X. Luo, H. Zhang, S. Wang, X. Duan, *Environ Sci Technol* **2022**, *56*, 78-97.
- [5] a) X. Cheng, H. Guo, Y. Zhang, G. V. Korshin, B. Yang, *Water Res* **2019**, *157*, 406-414; b) E. T. Yun, J. H. Lee, J. Kim, H. D. Park, J. Lee, *Environ Sci Technol* **2018**, *52*, 7032-7042.
- [6] W. Ren, G. Nie, P. Zhou, H. Zhang, X. Duan, S. Wang, *Environ Sci Technol* **2020**, *54*, 6438-6447.
- [7] L. Du, W. Xu, S. Liu, X. Li, D. Huang, X. Tan, Y. Liu, *Journal of Colloid and Interface Science* **2020**, *577*, 419-430.
- [8] Y. Gao, C. Yang, M. Zhou, C. He, S. Cao, Y. Long, S. Li, Y. Lin, P. Zhu, C. Cheng, *Small* **2020**, *16*, e2005060.
- [9] a) Y. Shang, X. Xu, B. Gao, S. Wang, X. Duan, *Chem Soc Rev* **2021**, *50*, 5281-5322; b) N. Zhang, C. Ye, H. Yan, L. Li, H. He, D. Wang, Y. Li, *Nano Research* **2020**, *13*, 3165-3182.
- [10] a) Z. Huang, Y. Yao, J. Lu, C. Chen, W. Lu, S. Huang, W. Chen, *J Hazard Mater* **2016**, *301*, 214-221; b) P. Huang, S. Huang, S. A. Pantovich, A. D. Carl, T. G. Fenton, C. Caputo, R. L. Grimm, A. I. Frenkel, G. Li, *J Am Chem Soc* **2018**, *140*, 16042-16047; c) X. Li, X. Huang, S. Xi, S. Miao, J. Ding, W. Cai, S. Liu, X. Yang, H. Yang, J. Gao, J. Yang, Y. Huang, T. Zhang, B. Liu, *J Am Chem Soc* **2018**, *140*, 12469-12475; d) H. Xu, N. Jiang, D. Wang, L. Wang, Y. Song, Z. Chen, J. Ma, T. Zhang, *Applied Catalysis B: Environmental* **2020**, *263*; e) Y. Yang, G. Zeng, D. Huang, C. Zhang, D. He, C. Zhou, W. Wang, W. Xiong, B. Song, H. Yi, S. Ye, X. Ren, *Small* **2020**, *16*, e2001634.
- [11] C. Chu, J. Yang, X. Zhou, D. Huang, H. Qi, S. Weon, J. Li, M. Elimelech, A. Wang, J. H. Kim, *Environ Sci Technol* **2021**, *55*, 1242-1250.
- [12] X. Mi, P. Wang, S. Xu, L. Su, H. Zhong, H. Wang, Y. Li, S. Zhan, *Angewandte Chemie International Edition* **2021**, *60*, 4588-4593.
- [13] a) X. Wu, H. Zhang, S. Zuo, J. Dong, Y. Li, J. Zhang, Y. Han, *Nano-Micro Letters* **2021**, *13*; b) L. Liu, A. Corma, *Chem Rev* **2018**, *118*, 4981-5079.
- [14] a) X. Dong, Z. Chen, A. Tang, D. D. Dionysiou, H. Yang, *Advanced Functional Materials* **2022**; b) H. Jin, P. Li, P. Cui, J. Shi, W. Zhou, X. Yu, W. Song, C. Cao, *Nat Commun* **2022**, *13*, 723.
- [15] a) Y. Wu, C. Chen, X. Yan, X. Sun, Q. Zhu, P. Li, Y. Li, S. Liu, J. Ma, Y. Huang, B. Han, *Angew Chem Int Ed Engl* **2021**, *60*, 20803-20810; b) C. Tang, Y. Jiao, B. Shi, J. N. Liu, Z. Xie, X. Chen, Q. Zhang, S. Z. Qiao, *Angew Chem Int Ed Engl* **2020**, *59*, 9171-9176; c) J. Zhang, Y. Zhao, C. Chen, Y. C. Huang, C. L. Dong, C. J. Chen, R. S. Liu, C. Wang, K. Yan, Y. Li, G. Wang, *J Am Chem Soc* **2019**, *141*, 20118-20126.
- [16] E. Jung, H. Shin, B. H. Lee, V. Efremov, S. Lee, H. S. Lee, J. Kim, W. Hooch Antink, S. Park, K. S. Lee, S. P. Cho, J. S. Yoo, Y. E. Sung, T. Hyeon, *Nat Mater* **2020**, *19*, 436-442.
- [17] C. Tang, L. Chen, H. Li, L. Li, Y. Jiao, Y. Zheng, H. Xu, K. Davey, S. Z. Qiao, *J Am Chem Soc* **2021**, *143*, 7819-7827.
- [18] L. Deng, L. Qiu, R. Hu, L. Yao, Z. Zheng, X. Ren, Y. Li, C. He, *Applied Catalysis B: Environmental* **2022**, *305*.
- [19] a) Y. Gao, Y. Zhu, L. Lyu, Q. Zeng, X. Xing, C. Hu, *Environ Sci Technol* **2018**, *52*, 14371-14380; b) Y. Gao, T. Wu, C. Yang, C. Ma, Z. Zhao, Z. Wu, S. Cao, W. Geng, Y. Wang, Y. Yao, Y. Zhang, C. Cheng, *Angew Chem Int Ed Engl* **2021**, *60*, 22513-22521.
- [20] J. Wang, B. Li, Y. Li, X. Fan, F. Zhang, G. Zhang, W. Peng, *Adv Sci (Weinh)* **2021**, *8*, e2101824.
- [21] P. Zhang, Y. Yang, X. Duan, Y. Liu, S. Wang, *ACS Catalysis* **2021**, *11*, 11129-11159.
- [22] B. Wu, L. Zhang, B. Jiang, Q. Li, C. Tian, Y. Xie, W. Li, H. Fu, *Angew Chem Int Ed Engl* **2021**, *60*, 4815-4822.
- [23] a) Y. S. Jun, J. Park, S. U. Lee, A. Thomas, W. H. Hong, G. D. Stucky, *Angew Chem Int Ed Engl* **2013**, *52*, 11083-11087; b) J.-W. Zhang, S. Gong, N. Mahmood, L. Pan, X. Zhang, J.-J. Zou, *Applied Catalysis B: Environmental* **2018**, *221*, 9-16.
- [24] S. An, G. Zhang, T. Wang, W. Zhang, K. Li, C. Song, J. T. Miller, S. Miao, L. Wang, X. Guo, *ACS Nano* **2018**, *12*, 9441-9450.
- [25] X. Hai, S. Xi, S. Mitchell, K. Harrath, H. Xu, D. F. Akl, D. Kong, J. Li, Z. Lin, Sun, H. Yang, Y. Cui, C. Su, X. Zhao, J. Li, J. Perez-Ramirez, J. Lu, *Nat Nanotechnol* **2022**, *17*, 174-181.
- [26] Y. Xiao, Y. Gao, L. Zhang, J. Zhang, Q. Zhang, Q. Li, H. Zhang, J. Zhou, S. Miao, N. Chen, J. Wang, B. Jiang, C. Tian, H. Fu, *Adv Mater* **2020**, *32*, e2003082.
- [27] J. Li, J. Shen, Z. Hong, B. Lin, B. Gao, Y. Chen, *Chem Commun (Camb)* **2012**, *48*, 12017-12019.
- [28] Y. Zeng, X. Liu, C. Liu, L. Wang, Y. Xia, S. Zhang, S. Luo, Y. Pei, *Applied Catalysis B: Environmental* **2018**, *224*, 1-9.
- [29] C. Chu, Q. Zhu, Z. Pan, S. Gupta, D. Huang, Y. Du, S. Weon, Y. Wu, C. Muhich, E. Stavitski, K. Domen, J. H. Kim, *Proc Natl Acad Sci U S A* **2020**, *117*, 6376-6382.
- [30] a) C. Wang, S. Mao, Z. Wang, Y. Chen, W. Yuan, Y. Ou, H. Zhang, Y. Gong, Y. Wang, B. Mei, Z. Jiang, Y. Wang, *Chem* **2020**, *6*, 752-765; b) Y. Yin, L. Shi, W. Li, X. Li, H. Wu, Z. Ao, W. Tian, S. Liu, S. Wang, H. Sun, *Environ Sci Technol* **2019**, *53*, 11391-11400.
- [31] N. Li, R. Li, X. Duan, B. Yan, W. Liu, Z. Cheng, G. Chen, L. a. Hou, S. Wang, *Environmental Science & Technology* **2021**, *55*, 16163-16174.
- [32] N. Li, R. Li, X. Duan, B. Yan, W. Liu, Z. Cheng, G. Chen, L. Hou, S. Wang, *Environ Sci Technol* **2021**, *55*, 16163-16174.
- [33] Z. Wang, H. Wang, Z. Zeng, G. Zeng, P. Xu, R. Xiao, D. Huang, X. Chen, L. He, C. Zhou, Y. Yang, Z. Wang, W. Wang, W. Xiong, *Applied Catalysis B: Environmental* **2020**, *267*.
- [34] Y. Gao, Z. Chen, Y. Zhu, T. Li, C. Hu, *Environ Sci Technol* **2020**, *54*, 1232-1241.
- [35] a) F. Chen, L. L. Liu, J. J. Chen, W. W. Li, Y. P. Chen, Y. J. Zhang, J. H. Wu, S. C. Mei, Q. Yang, H. Q. Yu, *Water Res* **2021**, *191*, 116799; b) J. Wang, J. Yu, Q. Fu, H. Yang, Q. Tong, Z. Hao, G. Ouyang, *ACS Cent Sci* **2021**, *7*, 355-364.
- [36] a) Y. Wu, C. F. Fu, Q. Huang, P. Zhang, P. Cui, J. Ran, J. Yang, T. Xu, *ACS Nano* **2021**, *15*, 7586-7595; b) J. Xu, X. Zheng, Z. Feng, Z. Lu, Z. Zhang, W. Huang, Y. Li, D. Vuckovic, Y. Li, S. Dai, G. Chen, K. Wang, H. Wang, J. K. Chen, W. Mitch, Y. Cui, *Nat Sustain* **2021**, *4*, 233-241; c) Y. Zou, K. Xiao, Q. Qin, J. W. Shi, T. Heil, Y. Markushyna, L. Jiang, M. Antonietti, A. Savateev, *ACS Nano* **2021**, *15*, 6551-6561.